View Article Online
View Journal

EES Solar

This article can be cited before page numbers have been issued, to do this please use: K. Radetzky, A. Garcia-Fernandez, B. Kammlander, E. Johannesson, B. Rydgren, R. M. Varma, H. Rensmo and U. B. Cappel, *EES Sol.*, 2026, DOI: 10.1039/D6EL00029K.

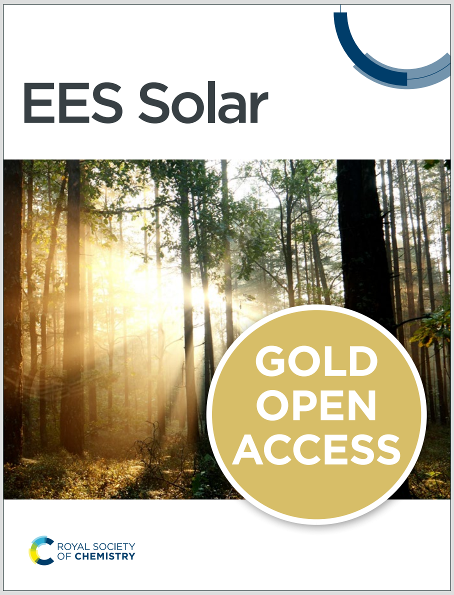

View Article Online
DOI: 10.1039/D6EL00029K

Broader context

Perovskite solar cells are a leading candidate for next-generation renewable energy, and both their efficiency and stability depend critically on the control of the interfaces between the perovskite and adjacent layers. P-i-n architectures, where the electron transport material are deposited on top of the perovskite are promising due to low temperature processing and the compatibility with silicon in a tandem solar cell architecture. In this study, we investigate both the energetic landscape and the chemistry of the interfaces formed between a perovskite absorber (methylammonium lead iodide) and the most common top contacting layers (a combination of C_{60}, bathocuproine (BCP), and silver) under highly controlled conditions. We find that the addition of BCP has a positive effect on the interface energy alignment. However, the addition of silver as the contacting metal can lead to chemical reactions, such as perovskite ion migration and lead reduction, which could cause device degradation. Some of these reactions can be prevented by a sufficiently thick BCP layer, which can cause a complexation of silver cations at the interface. These findings highlight the complexity of the possible interface reactions in a perovskite solar cell.

View Article Online
DOI: 10.1039/D6EL00029K

Journal Name

ARTICLE TYPE

Cite this: DOI: 00.0000/xxxxxxxxxx

Energetics and chemistry at the electron selective interfaces for p-i-n perovskite solar cells: an in situ investigation†

Karen Radetzky,[a,b] Alberto García Fernández,[a,c] Birgit Kammlander,[a] Evelyn Johannesson,[a,b] Brian Rydgren,[a,b] Rahul Mahavir Varma,[a] Håkan Rensmo,[a,b] and Ute B. Cappel*[a,b]

Received Date
Accepted Date

DOI: 00.0000/xxxxxxxxxx

Perovskite solar cells in an inverted p-i-n architecture are of high interest for developing efficient and affordable single junction photovoltaics and tandem devices. However, commercialization efforts are hampered by low operational stability, largely driven by chemical and electronic changes at critical interfaces, where reactions, ion migration, and energy misalignment can accelerate degradation. Understanding the interfacial chemistry, energetic alignment, and degradation pathways is therefore of primary importance to locate targets for material development and design. In this study, we investigate a partial device structure with clean interfaces, based on single crystal substrates and layers prepared under high-vacuum conditions. Specifically, we present a fully in situ assembled model system for an inverted p-i-n solar cell, extending from the absorber to the back contact. The architecture employs a $MAPbI_3$ (MA = methylammonium) single crystal as the absorber, with sequentially evaporated layers of C_{60}, bathocuproine (BCP), and silver. After each deposition, the material stack is immediately characterized in situ using photoelectron spectroscopy thereby allowing us to directly study the chemical and energetic changes occurring upon interface formation. We find stable interfaces upon deposition of the organic molecules and favorable downward energetic realignment of C_{60} by 0.3 eV toward the interface with BCP. However, the stability of the final half-cell is limited by reactions of the perovskite occurring upon silver evaporation. We observevethe permeation of the perovskite lead cation and iodide into the charge transport layers, as well as the formation of metallic lead. Only the latter can be inhibited by sufficiently thick BCP layers. Furthermore, a complex of cationic silver with BCP is formed after the deposition of the terminal silver layer.

Introduction

Inspired by the first report of a perovskite in solar cell applications in 2009,[1] perovskite-based single junction solar cells now achieve high power conversion efficiencies exceeding 26%.[2,3] Lead halide perovskites are prevalently employed light absorber materials due to their beneficial optoelectronic properties such as band gap tunability, high absorption coefficients, and long charge diffusion lengths.[4,5] Key advantages in device fabrication are low material costs and scalable solution processing methods.[6] The traditional device architecture is based on an n-i-p junction when considering the device from transparent conductive oxide (TCO) to metal contact. However, p-i-n junction devices of an inverted architecture are also of high interest in research. Inverted architecture perovskite solar cells (PSCs) allow for lower processing temperatures, which reduces production costs and paves the way towards fabrication of flexible devices while retaining band gap tunability.[7] This is also advantageous in the fabrication of two-terminal tandem devices as the processing conditions of subsequent layers are limited by the stability of the underlying stack.[8,9] Typical p-i-n devices employ a TCO front contact adjacent to a hole transport material (HTM).[10,11] Examples of organic HTMs are polymers such as poly[bis(4-phenyl)(2,4,6-trimethylphenyl)amine] (PTAA) or self-assembled monolayers (SAMs) based on carbazoles with phosphonic acid anchoring groups such as 2PACz, ([2-(9H-carbazol-9-yl)ethyl]phosphonic acid).[12,13] Alternatively, metal oxides, for

---

[a] *Division of X-ray Photon Science, Department of Physics and Astronomy, Uppsala University, Box 534, 751 20 Uppsala, Sweden*
[b] *Wallenberg Initiative Materials Science for Sustainability, Department of Physics and Astronomy, Uppsala University, 751 20 Uppsala, Sweden*
[c] *Universidade da Coruña, CICA (Interdisciplinary Center for Chemistry and Biology), Department of Chemistry, Faculty of Science, As Carballeiras, s/n, Campus de Elviña 15071 A Coruña, Spain.*
* ute.cappel@physics.uu.se

† Supplementary Information available: [details of any supplementary information available should be included here]. See DOI: 00.0000/00000000.

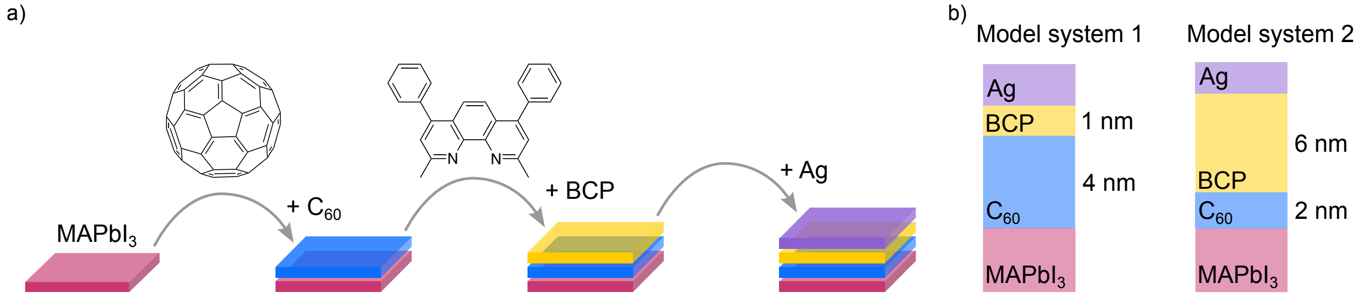

Fig. 1 Schematic showing a) the sequential fabrication of the p-i-n model system on a cleaved $MAPbI_3$ single crystal surface via in situ evaporation and b) the final model system configurations.

example based on nickel (NiO_x), are also investigated as HTMs.[14] Contacting the perovskite on the other side is the electron transport material (ETM), most commonly fullerene C_{60} or a derivative thereof with additional anchoring groups.[15] The ETM connects the perovskite to a metal back contact, such as silver. Often, additional buffer layers are introduced to optimize the device performance by defect passivation and hole blocking. For example, bathocuproine (BCP) is an insulator that is used at low thicknesses between the fullerene ETM and the metal contact.[16,17] This layer is attributed to improved charge separation and device stability.[18] It is suggested that charge transport across the insulator occurs through electron tunneling while holes are blocked due to disadvantageous energy alignment.[18] A remaining challenge in p-i-n PSCs is achieving prolonged device stability. Early on in the development of perovskite thin film devices, the high mobility of iodide in the bare perovskite was identified.[19] Halide diffusion and penetration through the ETM have also been shown for fully assembled PSCs.[20] Zhan et al. additionally report degradation of the silver contact under illumination by oxidation and diffusion into the perovskite bulk.[21] Electronically, the perovskite/C_{60} interface is associated with high recombination losses.[22,23] Moreover, the perovskite thin film coverage and crystallinity have been demonstrated to significantly depend on the thin film preparation and to affect the energetic alignment which impacted the overall device performance.[24] Therefore, understanding interfacial stability and energetic alignment is crucial to improving p-i-n junction devices.

In this work we investigate the interfacial chemistry in inverted architecture PSCs from the perovskite to the back contact. To focus on fundamental material interactions, this study was conducted on a methylammonium lead iodide ($MAPbI_3$) single crystal onto which layers of C_{60}, BCP, and silver were deposited via step-wise in situ thermal evaporation within the ultra high vacuum spectroscopy set-up. Compared to real devices, these model layers have a reduced thickness limited to a few nm. This enables us to continuously and directly monitor the underlying perovskite and establish the energy alignment and chemical changes occurring upon interface formation. Deposition onto a clean single crystal made it possible to study all phenomena independent of grain boundary effects and contamination. The assembled half cell was probed with photoelectron spectroscopy (PES). The experiments were conducted at a synchrotron light source (MAX IV, Sweden) in order to utilize soft X-rays of variable energy and maximize the signal gained from the organic components. Herein, all individual materials were monitored via their characteristic core levels. In this way, we were able to access qualitative information about the chemical nature of the species present and the energetic structure in the model device as well as quantitative information relating to degradation. We find a favorable energetic gradient via downward realignment of the C_{60} ETM at the interface with BCP. Additionally, we observe several degradation pathways which already impact the device stability in the assembly stage: We note a significant mobility not only of I^- but also of Pb^{2+} perovskite ions within the assembled charge transport layers and their accumulation at the metal contact. Furthermore, the formation of metallic lead upon silver evaporation is identified as a key decomposition reaction, which can be prevented through a sufficiently thick BCP layer.

Results and discussion

A sample matching the layer structure of the back half of a p-i-n PSC was assembled via thermal evaporation of C_{60}, BCP, and silver onto an in situ cleaved $MAPbI_3$ single crystal in two separate experiments producing two model systems, each with a unique set of layer thicknesses (Figure 1a, b). Photoelectron (PE) spectra were acquired after every evaporation to monitor each layer deposition. Synchrotron radiation enabled probing the fabricated stack at different information depths by tuning the incident photon energy to 758 eV, 535 eV, and 130 eV. Valence band measurements with 130 eV incident photon energy afforded high sensitivity to contributions from organic molecules. The complete set of spectra for both model systems is shown in Figures S2 - S9. If feasible, the layer thicknesses were calculated based on the attenuation of the Pb 4f core level intensities measured with 535 eV and 758 eV and are presented as the average of these results. The details and results of the calculations are described in Section 2 of the Supplementary Information. Although this publication primarily presents one main data set, important comparisons are discussed and additional measurements are shown in the Supplementary Information when differences due to the systems' configuration occurred. All shown spectra are energy calibrated to the Fermi level via measurement of a gold reference $(E_b(Au\ 4f_{7/2}) = 84.0\ eV,\ E_b(Au\ Fermi\ edge) = 0\ eV)$.[25] The individual layers were observed by measuring the valence band and characteristic core levels for each material, for instance Pb 4f and I 4d for $MAPbI_3$ and C 1s for C_{60} (Figures S2 - S7). BCP was

View Article Online
DOI: 10.1039/D6EL00029K

tracked via the N 1s PE peak while the silver layer was studied by recording Ag 3d core level spectra (Figures S8 - S9). In addition to the main measurement spot, a reduced number of selected PE spectra were acquired on a control spot to decouple independent phenomena from X-ray induced changes. Additionally all measurements were conducted in a looped sequence, to track possible X-ray induced changes over time. As the overlap between the C 1s and Pb 4f PE spectra of all measurement loops is good for all studied sample architectures, we assume the organic layers and perovskite to be stable under the experimental conditions (Figure S10). All PE spectra were fitted with a Pseudo-Voigt function and a Shirley or linear background to obtain the qualitative or quantitative information presented.

Clean $MAPbI_3$ single crystal surfaces were fabricated via blade cleaving under high vacuum conditions ($p = 1 \cdot 10^{-6} - 1 \cdot 10^{-8}$ mbar) and subsequently measured. All peaks in the recorded PE spectra can be attributed to the perovskite (Figure S11) and match well with our previous studies.[26] There is no indication of residual surface contamination by adventitious carbon or other oxygen-containing species resulting in a well controlled and defined sample surface for investigation. Furthermore, no evidence of the presence of metallic lead is observed in the Pb 4f PE spectra for the pristine surfaces. However, test measurements of the Pb 4f PE spectrum in three sampling positions on the primary crystal indicate a local variation in the peak position of up to 0.1 eV. We attribute this to charging effects or differences in surface termination.

Interface energetics in $MAPbI_3/C_{60}$

Figure 2 shows selected spectra of the $MAPbI_3$ single crystal before and after C_{60} evaporation for model system 1 - the full set of recorded spectra is shown in Figures S2 - S4. The Pb 4f core level peaks associated with Pb^{2+} in the $MAPbI_3$ single crystal ($E_b(Pb\ 4f_{7/2}) = 138.9\ eV$) decrease in intensity after the deposition of C_{60} (Figure 2a). From this peak attenuation, the final C_{60} layer thickness was calculated to be around 4 nm. To distinguish full surface coverage by C_{60} from island growth, we have predicted theoretical peak attenuation curves based on the initial Pb 4f intensity measured on the pristine perovskite for a series of fractional coverage values γ (details of the calculations can be found in the Supplementary Information). When comparing this to the fitted peak intensity actually measured after the evaporation of C_{60}, the data only intersects with the projected line that assumes full coverage (Figure 2b). The observed peak attenuation therefore supports a coverage of more than 90% of the underlying $MAPbI_3$ perovskite. The C 1s spectrum shows a sharp newly emerged main peak ($E_b(C\ 1s) = 285.1\ eV$) with smaller satellite features after the deposition of C_{60} whereas the MA C 1s feature is not discernible anymore (Figure 2c). The satellite peaks have a distinct separation (+ 1.9 eV and + 3.8 eV) from the main peak and are characteristic to shake-up processes in C_{60}. Our observation is in good agreement with established literature and serves as an indicator that the deposited molecules are intact.[27]

The second model system investigated here supports these conclusions and has a C_{60} overlayer of 2 nm thickness on a $MAPbI_3$ single crystal (Figures S5 - S7). Furthermore, this interface was the focus of earlier work, where we found that both the perovskite and C_{60} remain intact upon evaporation.[28] In this previous study, we also found downward energetic realignment in the C_{60} towards the perovskite within the first few monolayers of C_{60} on the surface, i.e. an energetic gradient unfavorable for electron transfer away from the interface. In the present experiment, the Pb 4f peak position of the primary model system shifts to lower binding energy upon evaporation. However, this effect is only observed for this crystal and is assigned to a small amount of sample charging confirmed by measurements with different photon flux densities (Figure S12). The valence band spectrum measured at 130 eV incident X-ray energy has a very different shape compared to the bare perovskite (Figure 2d). The strong attenuation of the Pb 5d feature ($E_b(Pb\ 5d_{5/2}) = 19.8\ eV$) recorded in the same spectrum indicates a minor contribution from the perovskite phase, while the features below 15 eV binding energy show good agreement with the established valence band shape of C_{60}.[29] The low photon energy of 130 eV thus makes it possible to selectively investigate the energetic structure of the topmost layer with an enhanced sensitivity to carbon-based orbitals compared to valence band measurements with a higher photon energy (Figure S4).

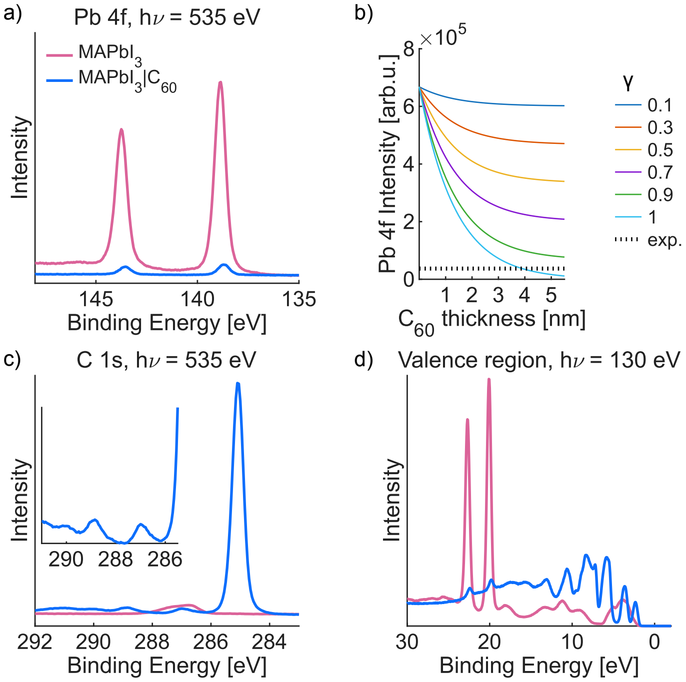

Fig. 2 Analysis of the C_{60} deposition. a) Pb 4f PE spectra of pristine $MAPbI_3$ (pink) and after C_{60} deposition (blue) measured with 535 eV incident photon energy. b) Projected Pb 4f peak intensity decay for different surface coverages γ. The experimentally determined value is indicated by the dashed line. c) C 1s PE spectra of pristine $MAPbI_3$ (pink) and after C_{60} deposition (blue) measured with 535 eV incident photon energy. d) Valence region spectra recorded with 130 eV incident photon energy on pristine $MAPbI_3$ (pink) and after the evaporation of C_{60} (blue).

View Article Online
DOI: 10.1039/D6EL00029K

Interface energetics in $MAPbI_3/C_{60}/BCP$

The deposition of C_{60} was followed by evaporation of BCP (Figure 3, Figures S2 - S4). The layer thickness was calculated from further peak attenuation of the Pb 4f feature and is approximately 1 nm for model system 1. This low thickness renders full coverage unlikely. The Pb 4f peak position is conserved and remains unaffected by the deposition. Similarly, the I 4d PE peaks reduce in intensity while the position and shape are conserved. Consequently, we conclude that there are no major changes to the perovskite after the deposition of a thin BCP layer. In model system 2, fabricated with 2 nm of C_{60}, the BCP layer was calculated to be 6 nm thick (Figures S5 - S7). In this case, the perovskite peaks are also conserved in position and shape after the evaporation of BCP and thus support the continued integrity of the $MAPbI_3$ single crystal in the case of thicker BCP layers. As the BCP molecule contains chemically distinct nitrogen atoms, the N 1s peak is used to confirm the deposition of BCP. For the first model system, a new N 1s peak is found at $E_b(N\ 1s) = 398.8\ eV$ binding energy (Figure 3a). This newly emerged sharp peak is significantly separate from the residual MA N 1s peak that has been dominant so far ($E_b(N\ 1s) = 402.6\ eV$). The measured N 1s binding energy of BCP is 399.3 eV at 6 nm BCP thickness, which represents a shift of + 0.5 eV from the peak position at 1 nm thickness (Figure S5). This variance with distance from C_{60} serves as an indicator that there is a upward shift of the BCP energetic levels towards the C_{60}/BCP interface or charging in the case of a thick layer.

Figure 3b shows the C 1s spectra recorded for model system 1 before and after the evaporation of 1 nm BCP. Because the C 1s features from BCP overlap significantly with the C_{60} C 1s main peak, the spectra contain both carbon signal from C_{60} and BCP. However, the C_{60} satellite features are still clearly discernible and continue to reveal information about the underlying C_{60}. For 6 nm thick BCP a broad C 1s with contributions from alkyl and aryl groups is measured at 285.7 eV binding energy (Figure S5). Residual signal from the C_{60} is not discernible. We have therefore focused on the core level data from the first model system in combination with valence band spectra to investigate the energetic alignment of C_{60} to BCP at the interface. Figure 3c shows the valence band spectra before and after the evaporation of 1 nm BCP calibrated to the Fermi level. Additionally, the valence band spectrum of the thick BCP layer (6 nm) is shown and serves as a reference to visualize the spectral envelope of BCP, while the spectrum before BCP evaporation shows the spectral features and energetics of C_{60} prior to BCP evaporation. To overlap the BCP reference spectrum correctly with the data from the primary model system, the reference spectrum was shifted under the assumption of a rigid band model meaning that the distance from the N 1s core level peak to the valence band is invariant (additional explanations provided in the Supplementary Information, Figure S13). Comparison of the spectra reveals that the onset of the BCP valence band feature is shifted by approximately + 0.5 eV to higher binding energy compared to the C_{60} valence band onset (Figure 3c). The shape of the valence band spectrum acquired on the first model system at 130 eV incident X-ray energy is therefore a sum of contributions from the BCP and C_{60} layers. Below 5 eV binding energy, two peaks are observed, matching with the presence of two peaks in the valence band of pure C_{60} in this energy range. However, the shape is distorted as the relative intensity changes due to contributions from BCP. The lower binding energy contribution to the density of states close to the Fermi energy still stems exclusively from C_{60} while contributions from BCP are only visible further away from the edge. The highest occupied molecular orbital (HOMO) of C_{60} remains discernible and shifts to higher binding energy after the deposition of BCP. As the characteristic C_{60} satellite peaks are visible in the C 1s spectrum (Figure 3b), we can use a rigid band model to quantify the shift in the C_{60} energy levels. This shift is + 0.3 eV and therefore significantly larger than the uncertainties in the Fermi level calibration of the experiment (0.1 eV). Within the rigid band assumption, the same shift applies to the HOMO and lowest unoccupied molecular orbital and thus represents downward energetic realignment in C_{60} towards the newly established C_{60}/BCP interface (Figure 3d). Overall, evaporation of a C_{60} ETM and an additional BCP blocking layer leads to energetic realignment at the interfaces. These newly formed interfaces are stable within the conditions and time scales of the experiment and no chemical reactions are observed.

Interface energetics and chemical changes in $MAPbI_3/C_{60}/BCP/Ag$

Silver was deposited via two consecutive evaporations for the model system with 1 nm BCP. This was confirmed via acquisition of Ag 3d PE spectra in which a distinct feature was observed ($E_b(Ag\ 3d_{5/2}) = 368.3\ eV$) (Figure S8). Moreover, the valence band measured with 535 eV is dominated by a new feature between 4 and 8 eV that is congruent with reports of the silver valence band in literature (Figure S4).[30] In addition, a distinct Fermi edge is observed which indicates that the newly formed layer is metallic. Despite the confirmed successful deposition of silver layers, the Pb 4f and I 4d perovskite PE peaks gain intensity in spectra acquired with 535 eV incident photon energy after the evaporation (Figure 4a, b). Hence, it is suggested that the perovskite ions migrate towards the surface and enter the charge transport layers. The assembled materials are permeable to both Pb^{2+} cations and I^- anions. On the control spot with reduced X-ray exposure, this increase in the Pb^{2+} associated Pb 4f PE peak after the evaporation of silver is also observed (Figure S14). X-ray exposure is therefore tentatively excluded as a driver for the observed perovskite ion diffusion. In agreement with this, the intensity of the I 4d core level peaks acquired with 758 eV incident photon energy grows after the evaporation of silver while the intensity of the Pb 4f core level peaks remains constant despite additional depositions (Figure 4c, d). As a result of the drastic ion movement, thickness determination of the silver layer based on the Pb 4f PE peak attenuation is not possible.

For model system 2 with a thicker layer of BCP of around 6 nm, silver was also evaporated in two consecutive cycles (Figure S9). We estimate that the final silver layer thickness is lower compared to the primary model system based on the Ag 3d PE peak intensity (see Figure S15 for details). When investigating the stability of the half cell with these modified layer thicknesses, we observe

View Article Online
DOI: 10.1039/D6EL00029K

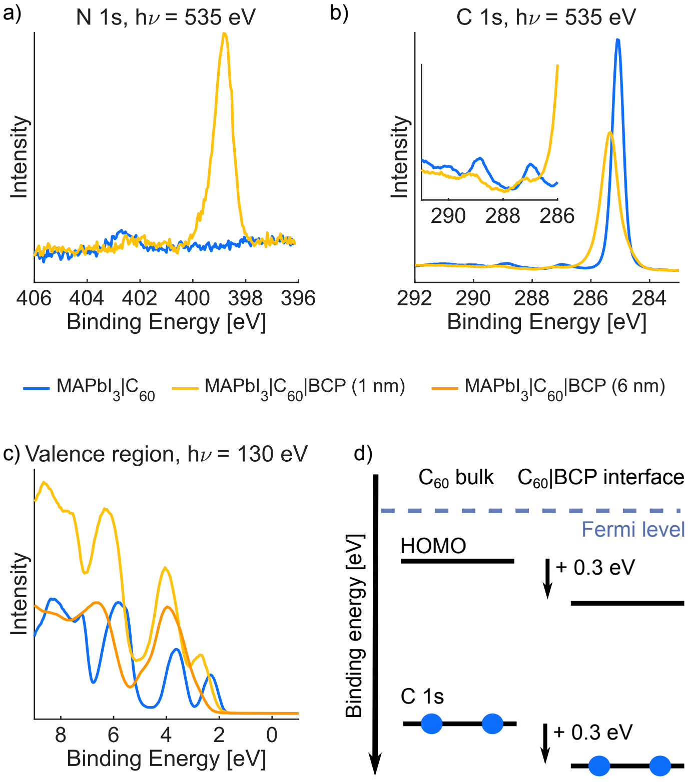

Fig. 3 Analysis of the BCP deposition. a) C 1s PE spectra and b) N 1s PE spectra acquired with 535 eV incident photon energy before (blue) and after (yellow) the deposition of BCP onto $MAPbI_3/C_{60}$ energy calibrated to the Fermi level. c) Valence region PE spectra acquired with 130 eV incident photon energy before and after the deposition of BCP of different thicknesses onto $MAPbI_3/C_{60}$. The spectra of $MAPbI_3/C_{60}$ (blue) and of $MAPbI_3/C_{60}$/BCP(1 nm) (yellow) are energy calibrated versus the Fermi level, while the spectrum of $MAPbI_3/C_{60}$/BCP(6 nm) is shifted to match with the energy position of BCP in $MAPbI_3/C_{60}$/BCP(1 nm) according to the rigid band model (see Supplementary Information). The reference spectra of $MAPbI_3/C_{60}$ (blue) and $MAPbI_3/C_{60}$/BCP(6 nm) (orange) are scaled so that the maximum intensity is one, the spectrum of $MAPbI_3/C_{60}$/BCP(1 nm) (yellow) is scaled so that the maximum intensity is two. d) Energetic diagram of C_{60} in the bulk and towards the interface with BCP.

an increase in intensity in the Pb 4f and I 4d peaks at both photon energies (Figure S16). Figure 4e and f summarize the relative changes in the core level peak intensity for the Pb^{2+} component of the Pb 4f core level peaks and the I 4d signal. The information depth can be approximated as three times the inelastic mean free path (IMFP). By using a simplified IMFP purely based on the universal curve, the resulting information depths are 3.2 nm and 4.0 nm for 535 eV and 758 eV incident photon energy when probing the Pb 4f core level.[31] Despite good general agreement in the intensity trend between both probing depths, the intensity of both perovskite ion peaks increases more in the more surface-sensitive measurements for both model systems. The peak intensity trends thus reveal that the ions accumulate close to the surface. Between the different probed ions, the intensity increase in the I 4d is stronger compared to the Pb 4f for the first model system: while the intensity of the Pb^{2+} component in the primary model system measured with 535 eV photon energy increases by a factor of 1.4, the I^- intensity increases by 2.7. This indicates that more iodide migrates compared to the lead cations. The data thus supports either faster migration or significantly longer diffusion lengths of I^- compared to Pb^{2+}. In the second model system, the Pb 4f intensity even decreases after the second silver deposition while the I 4d intensity continues to grow. Herein, the probing volumes with 535 eV and 758 eV both primarily access the BCP/Ag interface due to the large thickness of the BCP layer (6 nm). Based on this, build-up of perovskite ions in this segment is tentatively proposed. When comparing to the established literature, especially the migration of iodide is a well known phenomenon in $MAPbI_3$ based perovskite solar cells.[32,33] In contrast to this, the lead cations are often assumed as stationary due to the high activation energy for diffusion predicted by DFT calculations.[34–36] PES is a non-destructive, element-specific technique that enables the direct observation of Pb^{2+}. Despite the expected low mobility within the perovskite, we observe a significant migration of Pb^{2+} outside the perovskite phase and a high permeability of the adjacent electron selective layers in this experiment.

In addition to the Pb^{2+} peaks associated with the $MAPbI_3$ perovskite, a signal from a new lead species appears at lower binding energies after the first silver evaporation in the Pb 4f PE spectrum (Figure 4a, c) for the first model system. The peak intensity of this doublet relative to the main feature increases after the second deposition of silver. The peak position indicates the formation of metallic lead which is a common perovskite degradation product ($E_b(Pb\ 4f_{7/2}) = 136.8\ eV$).[37] This could be due to downward migration of silver atoms toward the perovskite layer or a reaction with Pb^{2+} ions that have migrated to the surface. The same reaction is present with lower X-ray exposure, excluding beam-induced effects as a possible cause of the observed degradation (Figure S14). Additionally, it has been shown that the primary degradation pathway of $MAPbI_3$ single crystals under prolonged X-ray exposure is MAI radiolysis.[38] The formation of metallic lead is instead consistent with the previously reported degradation pathway of $MAPbI_3$ when silver is deposited directly onto the single crystal surface.[39] The presence of silver is therefore the key prerequisite for the formation of metallic lead in the model system. It has been shown that air exposure can re-oxidize metallic lead that has formed via the reaction of a metal with a lead halide perovskite.[40] This demonstrates that in situ, ultra-high vacuum conditions as chosen here are required to even detect this initial degradation reaction. Measurements at both information depths indicate an increasing content of metallic lead with consecutive evaporations of Ag (Figure 4g). However, a higher content of metallic lead is found toward the surface reaching up to 16.6% of the total amount of lead detected compared to only 7.2% in more bulk-sensitive measurements. We therefore propose that metallic lead is primarily formed at the contacting interface via the reduction of cationic lead by metallic silver. The deposition of the silver contact therefore induces $MAPbI_3$ decomposition via ion diffusion and a chemical reaction. For the model system with a 6 nm layer of BCP, no metallic lead was observed (Figure S16). At sufficient thicknesses, BCP can therefore act as a protective layer and prevent the reduction of lead ions. Despite control over the degradation reaction, engineering the BCP layer thickness can-

View Article Online
DOI: 10.1039/D6EL00029K

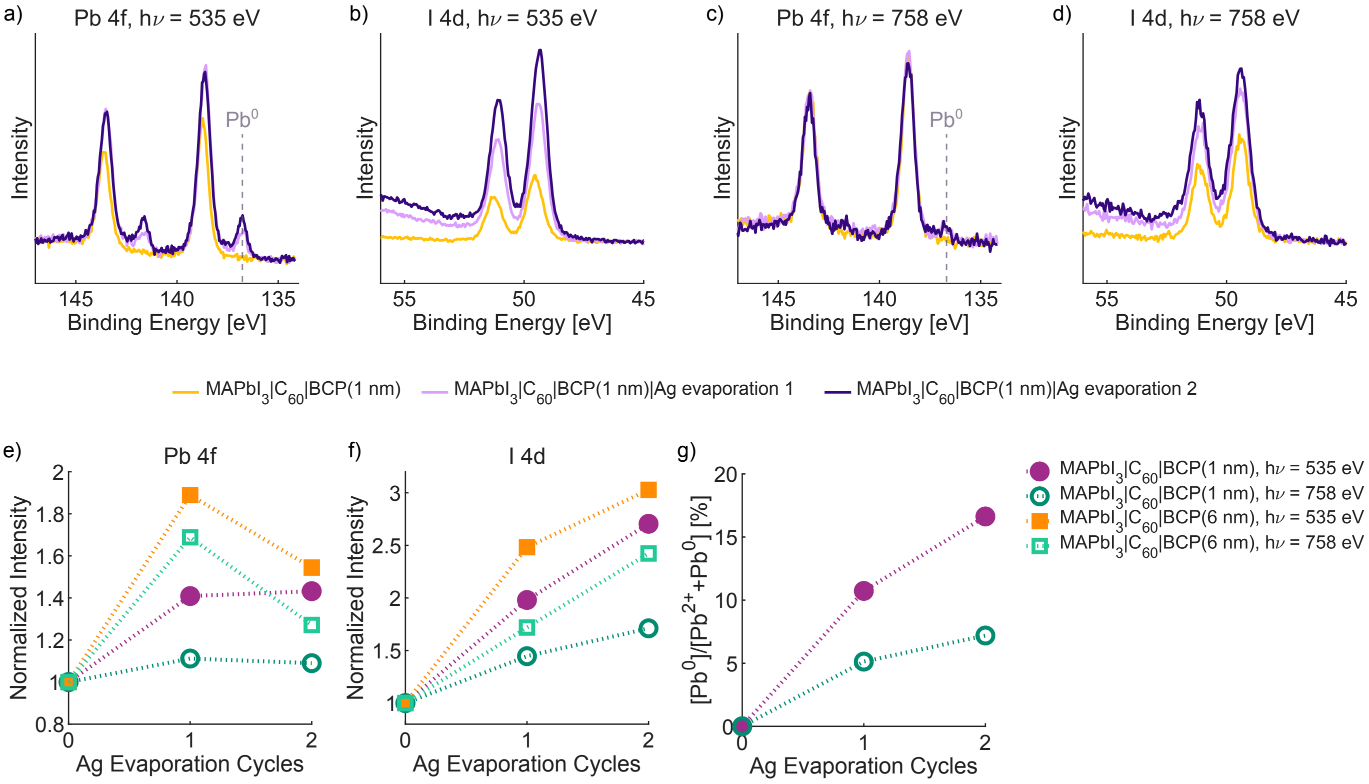

Fig. 4 Analysis of the Ag deposition. a) Pb 4f and b) I 4d PE spectra acquired before (yellow) and after (purple) consecutive evaporations of silver with a photon energy of 535 eV. c) Pb 4f and d) I 4d PE spectra acquired before (yellow) and after (purple) consecutive evaporations of silver with a photon energy of 758 eV. The intensity of the e) Pb^{2+} associated Pb 4f and f) I 4d PE core level peaks before and after the deposition of silver on $MAPbI_3/C_{60}/BCP$(1 nm) (circles) and $MAPbI_3/C_{60}/BCP$(6 nm) (squares) measured with 535 eV (filled) and 758 eV (empty) incident photon energy. To compare the presented data, all values are normalized to the intensity before silver deposition. g) The percentage of metallic lead of the overall lead detected related to the number of silver evaporations at the sample surface measured with 535 eV (purple) and deeper within the sample acquired with 758 eV (green) incident photon energy.

not mitigate the high mobility of the perovskite ions as discussed above.

Finally, there are significant changes in the BCP N 1s core level spectra acquired after the evaporation of silver (Figure 5a). Firstly, the N 1s main peak shifts by + 0.5 eV to higher binding energy for model system 1. The new peak position agrees well with reference measurements of BCP on a metallic Ag foil (Figure S17). Additionally, the peak becomes broader. We can therefore assign these observations to lowering of the BCP energy at the interface with metallic silver, spreading out the distribution of binding energies measured. Attribution of these effects to sample charging can be excluded based on measurements with different photon flux values (Figure S12).

For the second model system with a thicker layer of BCP of around 6 nm, the absolute energy calibration as described above is less reliable due to the low conductivity of BCP. However, a comparable shift of the N 1s peak by + 0.6 eV after the evaporation of a silver back contact is observed (Figure 5b). The BCP C 1s peak recorded with 535 eV and 758 eV as well as the BCP valence band features recorded with 130 eV incident photon energy also shift by + 0.6 eV and thus support the energetic change within the BCP, as the addition of Ag is unlikely to cause additional sample charging (Figure S5 - S7).

A further difference is a new N 1s feature emerging at higher binding energies ($E_b(N\ 1s) = 401.2\ eV$) for the model system with a 6 nm thick BCP layer (Figure 5b). For the thinner BCP layer, no equally distinctive new feature is observed (Figure 5a). However, the same additional peak is observed if the substrate is an Au-foil instead of a $MAPbI_3$ single crystal (Figure 5c), and it can therefore be excluded that the feature stems from MA cations that diffuse towards the surface. The origin of the peak must therefore be a chemically different species related to BCP - the only molecule containing nitrogen present in this highly controlled in situ fabrication process. We suggest, that this modification stems from a substrate-independent interaction between silver and BCP, namely the complexation of a silver species by the bipyridine unit in BCP, wherein the N atoms donate electronic density to the metal. Based on the relative intensity of the new feature to the main BCP associated N 1s peak, it is unlikely that the complexes form a continuous separating layer between pure BCP and silver at the interface (see Supplementary Information, Section 2.1). To learn more about the coordination compound, the shape of the more chemically sensitive Ag MNN Auger peak was compared for both model systems and a reference metallic silver foil (Figure 5d). While there is good agreement between the reference foil and the model system with a thinner BCP layer, the shape of the Ag MNN peak deviates strongly for the secondary model system with a thicker BCP layer and can therefore not be attributed

View Article Online
DOI: 10.1039/D6EL00029K

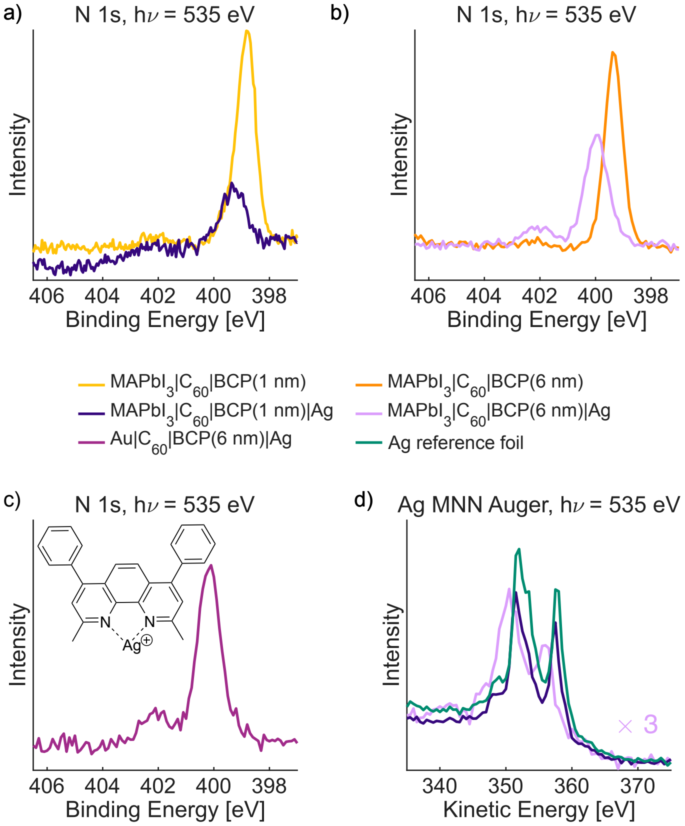

Fig. 5 N 1s PE spectra acquired with 535 eV incident photon energy before and after the deposition of silver on a) $MAPbI_3/C_{60}/BCP$(1 nm) and b) $MAPbI_3/C_{60}/BCP$(6 nm). c) N 1s PE spectra acquired with 535 eV incident photon energy after the deposition of silver on $Au/C_{60}/BCP$(6 nm). The structure of the suggested BCP complex with silver is shown. d) Auger MNN feature acquired at 535 eV incident photon energy. The shape indicates the oxidation state of silver to be +I (light purple) and 0 (dark purple and green).

to metallic silver. In accordance with established literature, this shape is instead associated with cationic silver.[41] Moreover, no distinct Fermi edge was observed after the evaporation of silver onto model system 2, which serves to support that the silver layer on top of the 6 nm BCP layer is not metallic (Figure S18). Instead, just a small trailing electronic density is observed close to the Fermi level. Sakurai et al. measured ultraviolet PES on Ag-doped BCP and found occupied gap states close to the Fermi level.[42] Yoshida additionally reports electronic density close to the Fermi level and assigns this to the HOMO of a BCP-Ag complex identified by theoretical calculations.[43] Our finding is therefore in good agreement with previous reports. Expanding on this current understanding and based on the thus far presented PES data we propose that the silver is specifically complexed as a monocation. While Ying et al. have reported a cationic complex previously,[44] we have been able to demonstrate the presence of the complex next to unreacted BCP as well as a definite determination of the silver oxidation state for the first time. Gong et al. report complexation of Ag with 4,4'-dicyano-2,2'-bipyridine (DCBP) which has the same structural bipyridine motive as BCP.[45] They propose a chelating effect induced by the two nitrogen atoms and subsequent release of an electron from the coordinated silver leading to an n - doping effect of the material. The elevation of the Fermi level would result in an increase in the measured binding energy and could therefore be an explanation for the shift in the BCP core levels we record in the presence of silver. Based on the valence region spectrum measured with a photon energy of 535 eV we exclude AgI as the prevalent Ag^+ containing species because the shape is not congruent with prior reports (Figure S7).[46]

Interface formation and energy alignment of the electron selective layers of p-i-n perovskite solar cells

In this section, we contextualize our findings on the formation and properties of the studied interfaces in terms of their implications for p-i-n perovskite solar cells. Figure 6 summarizes the observed phenomena. The energetic alignment of C_{60} to the $MAPbI_3$ perovskite was determined in previous studies[28,47] and presents a site for recombination due to an unfavorable energy gradient resulting in a barrier for electron transport away from the interface. While typical full devices employ C_{60} layer thicknesses between 25 nm and 40 nm,[3,48,49] efficient charge extraction has been shown for C_{60} layers as thin as 1 nm.[50] Especially considering the full coverage, the thin layers deposited here are sufficient to study the initial energetic alignment and establish the functionality of the layer despite a maximum thickness, which is thinner than in a typical device. The determined energetic shift of C_{60} is mitigated by the deposition of 1 nm of BCP which leads to a flattening of the C_{60} energy states. Wang et al. report qualitatively consistent results for depositing C_{60} onto BCP studied with ultraviolet photoemission spectroscopy.[51] The observed energetic gradient would be beneficial for guiding electron transport from C_{60} towards the interface with BCP in a real solar cell device. Furthermore, it might counteract the band bending in C_{60} towards the perovskite.

After deposition of silver, the energy level of BCP is in turn shifted downward, which should be favorable for electron extraction from C_{60} to silver through the BCP layer. The increased offset to the C_{60} HOMO should also block undesired hole transport. BCP buffer layers in PSCs usually have thicknesses of up to 8 nm in p-i-n PSCs.[16,49] In the presented two model systems, we are thus focusing on thicknesses close to the lower and upper limits of full device applications. While there are studies investigating the overall device performance as a function of BCP thickness,[16,18] our study provides insights into the energetic changes and chemical reactions at the BCP interfaces occurring upon formation.

After the deposition of silver, migration of I^- and even Pb^{2+} is observed through an increase in their core level intensity for both model systems studied. This indicates high ion mobility through the assembled electron transport layers and the degradation of the underlying $MAPbI_3$ perovskite. This suggests that ion rearrangement can already occur upon interface formation prior to device operation. While the migration of iodide has been previously reported,[32–34] the migration of lead ions is not typically considered. Moreover, the presence of metallic lead is observed close to the sample surface for very thin BCP layers. This degradation process can potentially be prevented by using thicker BCP

View Article Online
DOI: 10.1039/D6EL00029K

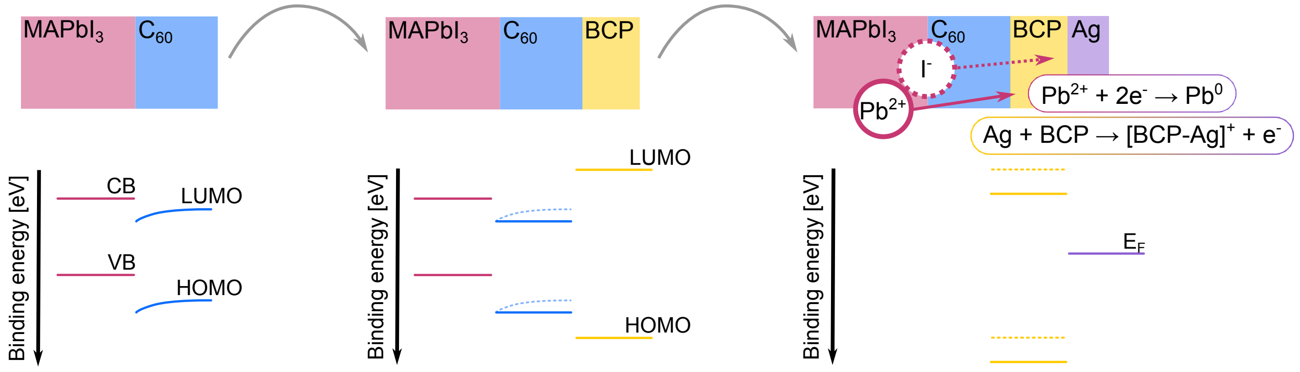

Fig. 6 Schematic summary of the changes observed in the energetic alignment upon interface formation including energy levels before (dashed) and after (solid) the addition of an extra layer. The chemical reactions occurring upon silver evaporation in a $MAPbI_3/C_{60}$/BCP/Ag p-i-n model system are also shown.

layers, as it was not observed in the second model system, where the BCP thickness was 6 nm. Furthermore, a quantitatively significant complexation reaction between silver and BCP is observed. The formation of this complex coincides with the oxidation of Ag, and is likely to be present at the BCP interface with silver in complete solar cells, where it would impact the energy alignment at the interface.

As the $MAPbI_3$ poses the major obstacle to device stability, we were also interested in how our results apply to systems with formamidinium (FA) iodide-based perovskites, which are typically employed in the most efficient perovskite solar cells.[52,53] A comparison to a single crystal of mixed cation $Cs_xFA_{1-x}PbI_3$ is presented in Section 4 of the Supplementary Information (Figures S19 - S24). In this case, comparable layer thicknesses as in the second model system were evaporated and similar chemical changes were observed upon silver evaporation. Overall, the data supports the migration of Pb^{2+} and iodide outside the perovskite phase after the deposition of silver. The formation of a complex consisting of BCP coordinating to a silver monocation is also confirmed. This suggests that the chemical reactions occurring upon silver evaporation are of relevance for both PSCs based on methylammonium cations as well as for those based on formamidinium cations.

Conclusions

The presented experiment demonstrates the successful in situ assembly and characterization of a p-i-n solar cell model system based on a $MAPbI_3$ single crystal with layers of C_{60}, BCP, and Ag deposited via thermal evaporation. Photoelectron spectroscopy measurements reveal energetic realignment by 0.3 eV of C_{60} at the interface with BCP, as well as an energetic realignment of BCP in presence of silver, which both favor guided charge transport. Furthermore, the stability of the model system was studied. While the evaporation of C_{60} and BCP produced chemically inert interfaces, the degradation of $MAPbI_3$ is indicated by the formation of metallic lead after the evaporation of silver. The results support that the decomposition can be prevented given a sufficient thickness of the BCP buffer layer. In this case, complexation of silver as a monocation by the bipyridine unit has been observed. Additionally, the electron transporting materials are permeable to the Pb^{2+} and I^- ions which can leave the underlying perovskite phase and migrate toward the metal contact. Particularly, accumulation of ions within the probed BCP/Ag segment is observed. However, due to the use of a $MAPbI_3$ single crystal we identify the fundamental perovskite material as the limiting component in the final device stability independent of other fabrication parameters such as film quality. The observed degradation phenomena are already present during assembly without any additional exposure to ambient conditions and can also occur for formamidinium-based perovskites. This stresses the need to protect the lead halide absorber and to develop strategies to prevent ion migration while conserving favorable energetic alignment. As the herein developed model system approach provides valuable insight into device stability and energetics, the goal of future investigations will be to examine these interfaces under illumination. Such studies will link our present study focused on interface formation to changes occurring under operating conditions. The presented method is applicable to any stack of interfaces that allows for in situ deposition and could be useful in other research areas.

Experimental

Single crystal synthesis

$MAPbI_3$ single crystals were fabricated via inverse temperature crystallization,[54,55] as described previously:[26] PbI_2 and MAI were combined at an equimolar ratio in γ-butyrolactone to make a 1 M solution. The solution was stirred at 50 °C. After full dissolution of the precursor materials, the solution was filtered using a 0.45 μm PTFE filter, transferred to an open glass vial and heated to 100 °C. Single crystals formed and were removed from solution. The final diameter of the single crystals is about 5 mm - 10 mm.

Photoelectron spectroscopy measurements

Photoelectron spectra were recorded at the Surface and Material Science branch of the FlexPES beamline, MAX IV, Sweden.[56] A plane grating monochromator (modified Zeiss SX700) was used to tune the X-ray beam energy from the undulator source to 130 eV for valence band characterization and 535 eV or 758 eV for

View Article Online
DOI: 10.1039/D6EL00029K

core level measurements. Unless otherwise specified, the exit slit was set to 10 μm for 535 eV incident photon energy and to 5 μm for 758 eV and 130 eV. All spectroscopy measurements were conducted under ultra high vacuum conditions in the main chamber ($p = 1 \cdot 10^{-9} - 1 \cdot 10^{-10}$mbar). To prevent sample degradation under incident X-ray irradiation, the beam was defocused with a final spot size of approximately 1 mm × 0.4 mm. Photoelectrons were measured using a Scienta DA30-L(W) spectrometer and a 40 mm MCP/CCD detector. The spectrometer slit was set to 0.5 mm. Core level spectra were acquired with a 100 meV step size and 100 eV pass energy. The Ag MNN Auger peak was acquired with 500 meV step size. The acquired data was fitted using Pseudo-Voigt functions in combination with a linear or Shirley background. Quantitative relationships were determined by dividing the intensity measured by the core level specific photoionization cross section.[57] To assess effects of beam damage or beam induced behavior, a secondary spot was measured with reduced X-ray exposure (approximately 15% of the main spot). This was achieved by limiting the characterization to measurements with 535 eV incident photon energy and reducing the number of core levels measured. The impact of sample charging was assessed for model system 1 by measuring selected core levels with five different photon flux values in a different spot on the sample (Figure S12). Shifts were found to be lower than 0.1 eV and become negligible after the deposition of BCP.

Perovskite single crystals were mounted on the sample plate with two component conductive epoxy EPO-TEK H20E and cured at 100 °C for 1 h. The epoxy establishes a good electrical contact between the single crystal and the sample plate. A gold foil was mounted on the same sample plate and measured for energy calibration and the sample plate was grounded to the spectrometer during all measurements. Prior to measurement, the samples were cleaved with a blade cleaver under high vacuum conditions ($p = 1 \cdot 10^{-6} - 1 \cdot 10^{-8}$ mbar). Subsequent layers were deposited on the single crystal substrates and co-mounted gold foil from a molecular source in alumina boats (Ted Pella) heated in a thermal evaporator in the primary preparation chamber.

Author contributions

K.R.: Formal analysis, investigation, writing (Original draft, review, and editing), visualization A.G.-F.: Investigation, conceptualization, writing (Review and editing), Resources B.K.: Investigation, conceptualization, writing (Review and editing) E.J.: Investigation, writing (Review and editing) B.R.: Investigation, writing (Review and editing) R.M.V.: Investigation, writing (Review and editing) H.R.: Writing (Review and editing), funding acquisition U.B.C.: Writing (Review and editing), supervision, project administration, funding acquisition

Conflicts of interest

There are no conflicts to declare.

Data availability

The data supporting this article has been included as part of the Supplementary Information.

Acknowledgements

This work was partially supported by the Wallenberg Initiative Materials Science for Sustainability (WISE) funded by the Knut and Alice Wallenberg Foundation and the Swedish Research Council under registration numbers 2022-03168 and 2023-05072. The authors acknowledge the MAX IV Laboratory for beamtime on the Surface and Material Science branch of the FlexPES beamline under proposals 20230156 and 20240429. Research conducted at MAX IV, a Swedish national user facility, is supported by Vetenskapsrådet (Swedish Research Council, VR) under contract 2018-07152, Vinnova (Swedish Governmental Agency for Innovation Systems) under contract 2018-04969, and Formas under contract 2019-02496. A.G.-F. acknowledges support from a Beatriz Galindo junior fellowship (BG23/00033) from the Spanish Ministry of Science and Innovation. The authors kindly thank Alexei Preobrajenski, Stephan Appelfeller, and Alexander Generalov for their assistance and support during the measurement time.

References

1 A. Kojima, K. Teshima, Y. Shirai and T. Miyasaka, *Journal of the american chemical society*, 2009, **131**, 6050–6051.
2 Y. Wang, Z. Feng, Y. Zhang, H. Huang, Y. Guo, J. Xu, H. Zhang, Y. Ji, L. Li, C. Ge *et al.*, *Advanced Functional Materials*, 2025, e10458.
3 D. Wang, Z. Liu, Y. Qiao, Z. Jiang, P. Zhu, J. Zeng, W. Peng, Q. Lian, G. Qu, Y. Xu *et al.*, *Joule*, 2025, **9**, year.
4 E. Unger, L. Kegelmann, K. Suchan, D. Sörell, L. Korte and S. Albrecht, *Journal of Materials Chemistry A*, 2017, **5**, 11401–11409.
5 S. D. Stranks, G. E. Eperon, G. Grancini, C. Menelaou, M. J. Alcocer, T. Leijtens, L. M. Herz, A. Petrozza and H. J. Snaith, *Science*, 2013, **342**, 341–344.
6 J. Yan, T. J. Savenije, L. Mazzarella and O. Isabella, *Sustainable Energy & Fuels*, 2022, **6**, 243–266.
7 L. Meng, J. You, T.-F. Guo and Y. Yang, *Accounts of chemical research*, 2016, **49**, 155–165.
8 H. Li and W. Zhang, *Chemical Reviews*, 2020, **120**, 9835–9950.
9 P. Chen, Y. Xiao, S. Li, X. Jia, D. Luo, W. Zhang, H. J. Snaith, Q. Gong and R. Zhu, *Chemical Reviews*, 2024, **124**, 10623–10700.
10 T. Lemercier, L. Perrin, S. Berson, L. Flandin and E. Planes, *Materials Advances*, 2021, **2**, 7907–7921.
11 D. D. Astridge, J. B. Hoffman, F. Zhang, S. Y. Park, K. Zhu and A. Sellinger, *ACS Applied Polymer Materials*, 2021, **3**, 5578–5587.
12 J. Wang, J. Xu, Z. Li, X. Lin, C. Yu, H. Wu and H.-l. Wang, *ACS Applied Energy Materials*, 2020, **3**, 6344–6351.
13 A. Al-Ashouri, A. Magomedov, M. Roß, M. Jošt, M. Talaikis, G. Chistiakova, T. Bertram, J. A. Márquez, E. Köhnen, E. Kasparavičius *et al.*, *Energy & Environmental Science*, 2019, **12**, 3356–3369.
14 H. Sheng, Q. Zhao, X. Sun, B. Zhang, Q. Huang, K. Wang, L. Wang and S. Pang, *Solar RRL*, 2024, **8**, 2300779.

View Article Online
DOI: 10.1039/D6EL00029K

15 H. Wang, Z. Zhang, C. Zhang, Y. Yao and K. Wang, *Journal of Materials Chemistry A*, 2024.

16 N. Shibayama, H. Kanda, T. W. Kim, H. Segawa and S. Ito, *APL Materials*, 2019, **7**, year.

17 W. Li, G. Wang, Y. Long, L. Xiao, Z. Zhong, X. Li, H. Xu, H. Yan and Q. Song, *ACS Applied Materials & Interfaces*, 2024, **16**, 63019–63025.

18 C. Chen, S. Zhang, S. Wu, W. Zhang, H. Zhu, Z. Xiong, Y. Zhang and W. Chen, *RSC advances*, 2017, **7**, 35819–35826.

19 D. W. DeQuilettes, W. Zhang, V. M. Burlakov, D. J. Graham, T. Leijtens, A. Osherov, V. Bulović, H. J. Snaith, D. S. Ginger and S. D. Stranks, *Nature communications*, 2016, **7**, 11683.

20 M. Kim, H. Jun, H. Lee, H. Nahdi, D. Tondelier, Y. Bonnassieux, J.-É. Bourée and B. Geffroy, *European Journal of Inorganic Chemistry*, 2021, **2021**, 4781–4789.

21 C. Zhan, C. Luo, F. Gao, X. Wang, P. Gao, Y. Ma, K. Wang, J. He, Z. Bi, Y. Ma *et al.*, *Small*, 2025, 2502989.

22 M. Stolterfoht, P. Caprioglio, C. M. Wolff, J. A. Márquez, J. Nordmann, S. Zhang, D. Rothhardt, U. Hörmann, Y. Amir, A. Redinger *et al.*, *Energy & environmental science*, 2019, **12**, 2778–2788.

23 J. Warby, F. Zu, S. Zeiske, E. Gutierrez-Partida, L. Frohloff, S. Kahmann, K. Frohna, E. Mosconi, E. Radicchi, F. Lang *et al.*, *Advanced Energy Materials*, 2022, **12**, 2103567.

24 G. Li, Z. Su, L. Canil, D. Hughes, M. H. Aldamasy, J. Dagar, S. Trofimov, L. Wang, W. Zuo, J. J. Jerónimo-Rendon *et al.*, *Science*, 2023, **379**, 399–403.

25 R. Nyholm, A. Berndtsson and N. Martensson, *Journal of Physics C: Solid State Physics*, 1980, **13**, L1091.

26 A. García-Fernández, S. Svanström, C. M. Sterling, A. Gangan, A. Erbing, C. Kamal, T. Sloboda, B. Kammlander, G. J. Man, H. Rensmo *et al.*, *Small*, 2022, **18**, 2106450.

27 C. Enkvist, S. Lunell, B. Sjögren, S. Svensson, P. A. Brühwiler, A. Nilsson, A. J. Maxwell and N. Mårtensson, *Physical Review B*, 1993, **48**, 14629.

28 A. García-Fernández, K. Radetzky, S. Riva, B. Kammlander, B. Rydgren, E. Johannesson, R. M. Varma, H. Rensmo and U. B. Cappel, *Resolving the energy alignment between methylammonium lead iodide and C60: an in-situ photoelectron spectroscopy study*, 2026, `https://arxiv.org/abs/2601.07755`.

29 D. L. Lichtenberger, K. W. Nebesny, C. D. Ray, D. R. Huffman and L. D. Lamb, *Chemical physics letters*, 1991, **176**, 203–208.

30 G. Panaccione, G. Cautero, M. Cautero, A. Fondacaro, M. Grioni, P. Lacovig, G. Monaco, F. Offi, G. Paolicelli, M. Sacchi *et al.*, *Journal of Physics: Condensed Matter*, 2005, **17**, 2671.

31 M. P. Seah and W. Dench, *Surface and interface analysis*, 1979, **1**, 2–11.

32 C. Li, S. Tscheuschner, F. Paulus, P. E. Hopkinson, J. Kießling, A. Köhler, Y. Vaynzof and S. Huettner, *Advanced Materials*, 2016, **28**, 2446–2454.

33 J. M. Azpiroz, E. Mosconi, J. Bisquert and F. De Angelis, *Energy & Environmental Science*, 2015, **8**, 2118–2127.

34 C. Eames, J. M. Frost, P. R. Barnes, B. C. O'regan, A. Walsh and M. S. Islam, *Nature communications*, 2015, **6**, 7497.

35 J. S. Yun, J. Seidel, J. Kim, A. M. Soufiani, S. Huang, J. Lau, N. J. Jeon, S. I. Seok, M. A. Green and A. Ho-Baillie, *Advanced Energy Materials*, 2016, **6**, 1600330.

36 M. H. Futscher, J. M. Lee, L. McGovern, L. A. Muscarella, T. Wang, M. I. Haider, A. Fakharuddin, L. Schmidt-Mende and B. Ehrler, *Materials Horizons*, 2019, **6**, 1497–1503.

37 A. L. Abdelhady, S. N. Afraj, Y. Haruta, M. M. Uddin and M. I. Saidaminov, *ACS nano*, 2025, **19**, 35276–35305.

38 A. García-Fernández, B. Kammlander, S. Riva, H. Rensmo and U. B. Cappel, *Physical Chemistry Chemical Physics*, 2024, **26**, 1000–1010.

39 S. Riva, *PhD thesis*, Acta Universitatis Upsaliensis, 2025.

40 S. Svanström, A. García-Fernández, T. J. Jacobsson, I. Bidermane, T. Leitner, T. Sloboda, G. J. Man, G. Boschloo, E. M. J. Johansson, H. Rensmo and U. B. Cappel, *ACS Materials Au*, 2022, **2**, 301–312.

41 A. M. Ferraria, A. P. Carapeto and A. M. Botelho do Rego, *Vacuum*, 2012, **86**, 1988–1991.

42 T. Sakurai, S. Toyoshima, H. Kitazume, S. Masuda, H. Kato and K. Akimoto, *Journal of Applied Physics*, 2010, **107**, year.

43 H. Yoshida, *The Journal of Physical Chemistry C*, 2015, **119**, 24459–24464.

44 Z. Ying, X. Yang, J. Zheng, Y. Zhu, J. Xiu, W. Chen, C. Shou, J. Sheng, Y. Zeng, B. Yan, H. Pan, J. Ye and Z. He, *J. Mater. Chem. A*, 2021, **9**, 12009–12018.

45 C. Gong, H. Li, H. Wang, C. Zhang, Q. Zhuang, A. Wang, Z. Xu, W. Cai, R. Li, X. Li *et al.*, *Nature Communications*, 2024, **15**, 4922.

46 Y. Kato, L. K. Ono, M. V. Lee, S. Wang, S. R. Raga and Y. Qi, *Advanced Materials Interfaces*, 2015, **2**, 1500195.

47 C. Wang, C. Wang, X. Liu, J. Kauppi, Y. Shao, Z. Xiao, C. Bi, J. Huang and Y. Gao, *Applied physics letters*, 2015, **106**, year.

48 Z. Li, X. Sun, X. Zheng, B. Li, D. Gao, S. Zhang, X. Wu, S. Li, J. Gong, J. M. Luther *et al.*, *Science*, 2023, **382**, 284–289.

49 W. Zhou, H. Liu, H. Li, W. Zhang, H. Li, X. Zhou, R. Chen, W. Zhang, T. Shi, A. Abate *et al.*, *Nano-Micro Letters*, 2026, **18**, 157.

50 D. Liu, Q. Wang, C. J. Traverse, C. Yang, M. Young, P. S. Kuttipillai, S. Y. Lunt, T. W. Hamann and R. R. Lunt, *ACS nano*, 2018, **12**, 876–883.

51 S. Wang, T. Sakurai, R. Kuroda and K. Akimoto, *Applied physics letters*, 2012, **100**, year.

52 J. Wu, S. Yu, Z. Luo, Z. Zou, J. Zhou, T. Cui, L. Huang, W. Zhang, Y. Liu, L. Xiao *et al.*, *Advanced Functional Materials*, 2026, e26679.

53 Y. Zhang, Y. Chen, G. Liu, Y. Wu, Z. Guo, R. Fan, K. Li, H. Liu, Y. Zhao, T. Kodalle, Y. Chen, C. Zhu, Y. Bai, Q. Chen and H. Zhou, *Science*, 2025, **387**, 284–290.

54 M. I. Saidaminov, A. L. Abdelhady, B. Murali, E. Alarousu, V. M. Burlakov, W. Peng, I. Dursun, L. Wang, Y. He, G. Maculan *et al.*, *Nature communications*, 2015, **6**, 7586.

55 M. I. Saidaminov, A. L. Abdelhady, G. Maculan and O. M. Bakr, *Chemical communications*, 2015, **51**, 17658–17661.

56 A. Preobrajenski, A. Generalov, G. Öhrwall, M. Tchaplyguine,

View Article Online
DOI: 10.1039/D6EL00029K

H. Tarawneh, S. Appelfeller, E. Frampton and N. Walsh, *Synchrotron Radiation*, 2023, **30**, 831–840.

57 J. H. Scofield, *Theoretical photoionization cross sections from 1 to 1500 keV.*, California univ., livermore. lawrence livermore lab. technical report, 1973.

View Article Online
DOI: 10.1039/D6EL00029K

The data supporting this article has been included as part of the Supplementary Information.